# Photocatalytic degradation of textile reactive dye using artificial neural network modeling approach

G.G. Lenzi[a,*], R.F. Evangelista[c], E.R. Duarte[a], L.M.S. Colpini[b], A.C. Fornari[c], R. Menechini Neto[c], L.M.M. Jorge[c], O.A.A. Santos[c]

[a]*Departamento de Engenharia Química, Universidade Tecnológica Federal do Paraná, Av. Monteiro Lobato s/n, CEP, 84016-210 Ponta Grossa, Paraná, Brasil, Tel. +55 42 32204800; emails: gianegoncalves@hotmail.com (G.G. Lenzi), erduarte@ufpr.edu.br (E.R. Duarte)*
[b]*Departamento de Química, Universidade Federal do Paraná, Campus Avançado de Jandaia do Sul., Rua Doutor João Maximiano, 426, CEP, 86900-000 Jandaia do Sul, Paraná, Brasil, Tel. +55 43 3432 4658; email: ledasaracol@ufpr.br*
[c]*Departamento de Engenharia Química, Universidade Estadual de Maringá, Av. Colombo, 5790, CEP, 87020-900 Maringá, Paraná, Brasil, Tel. +55 44 3011 4770; emails: renatofeeq@gmail.com (R.F. Evangelista), ariellecfornari@hotmail.com (A.C. Fornari), menechini@yahoo.com.br (R. Menechini Neto), lmmj@deq.uem.br (L.M.M. Jorge), onelia@deq.uem.br (O.A.A. Santos)*

## ABSTRACT

This study describes the application of $TiO_2$, $ZnO$, $TiO_2$–$ZnO$-based systems modified with 1.5 and 2.5% wt. Fe using the impregnation method for the maxilon blue 5G dye discoloration. Specific surface area (BET method), X-ray diffraction, thermogravimetric analysis, and photoacoustic spectroscopy characterization techniques were used in this work. The presented results indicate that structure alterations, textural properties, nominal metallic charges, and photocatalyst thermal treatment affected the photocatalytic activity of the system. Moreover, all of the synthesized catalysts yielded complete discoloration of the maxilon blue 5G dye within 180 min of reaction. The reaction time required for total discoloration was strongly affected by the temperature of photocatalysts calcination. In general, increasing the catalysts nominal metallic charge improves the adsorption process. A neural model was developed for each studied catalyst using MLP network with three intermediate layers, backpropagation learning algorithm, and sigmoid activation function implemented in FORTRAN. The three models presented the best results with three neurons in the intermediate layer. Therefore, the neural networks can be successfully employed to model the discoloration process involving the synthesized catalyst ($R^2$ varying between 0.98 and 0.99).

*Keywords:* Photocatalytic reduction; Reactive maxilon blue 5G dye; Characterization; Artificial neural networks

## 1. Introduction

Dyes are colored substances majorly used in textile fibers and fabrics coloring to permanently transmit colors to other substances. They constitute an abundant class of organic compounds characterized by the presence of unsaturated groups (chromophores), such as –C≡C–, –N≡N–, and –C≡N–, responsible for dye colors—and functional groups—responsible for their fixation to fibers such as $NH_2$, –OH, –COOH,

*Corresponding author.

and –SO$_3$H [1]. The discoloration of dyehouse wastewaters is a major issue for the textile sector [2]; in this context, photocatalysis is a promising alternative to treat residual waters [3].

Superoxide anion radicals and hydroxyl radicals (·OH) generated in the aqueous medium (Eqs 2 and 3) are responsible for accelerating the oxidation of pollutants [4,5].

$$\text{Semiconductor} + \text{hv} \rightarrow e^- + h^+ \tag{1}$$

$$O_2 + e^- \rightarrow \cdot O_2^- \tag{2}$$

$$H_2O + h^+ \rightarrow \cdot OH + H^+ \tag{3}$$

$$OH^- + h^+ \rightarrow \cdot OH \tag{4}$$

$$\cdot OH + H^+ \rightarrow \cdot OH_2 \tag{5}$$
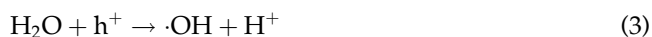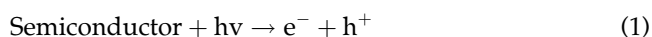
Overall, titanium dioxide (TiO$_2$) is the preferred photocatalyst for water detoxification because of its ability to decompose several organic pollutants [6,7]. Even though the TiO$_2$ anatase band gap is larger than ZnO band gap (3.2 against 3.17 eV), under certain conditions, ZnO is more effective than TiO$_2$. Daneshvar et al., (2007) reported that ZnO appears to be a suitable alternative to TiO$_2$ as it follows similar photodegradation mechanism with TiO$_2$ [8].

Moreover, introducing transition-metal ions into the TiO$_2$ enables the formation of doping conduction and valence bands, subsequently moving the band gap of TiO$_2$ to the visible region. A dopant ion is also able to act as a trap for electrons, which increases the TiO$_2$ catalytic activity under visible light irradiation [9,10]. However, the doped TiO$_2$ photoactivity depends on the preparation method, thermal treatment, nature of dopant ion, and its concentration [11]. Neural networks are mathematical models able to

learn and adapt, recognize and classify data by rapidly processing complex and nonlinear time-varying information [12]. The artificial neural networks (ANNs) are successfully employed as algorithms for solving problems of mapping, regression, modeling, multivariate data analysis, optimization, control classification, and chemical differentiation [13].

Many authors have used neural networks for the modeling of photocatalytic degradation process [14–16] due to its great robustness, which hampers the development of phenomenological models. In this context, the objective of this research is to investigate the effect of metal presence on the catalyst surface (1.5 and 2.5% wt. Fe) and calcination temperatures on TiO$_2$ and ZnO. The photocatalytic efficiency of blue 5G dye discoloration (Table 1 presents the structure and characteristics of maxilon blue 5G, which is widely used by the Brazilian textile industry [17]).

The influence of the basic operational parameters on the predictive capability of ANN modeling approach applied to the maxilon blue 5G dye degradation/photodiscoloration was also investigated

## 2. Experimental procedure

### 2.1. Preparation of photocatalysts

This section contains aims to describe the experimental methods and procedures to prepare the Fe/TiO$_2$, Fe/ZnO, and Fe/TiO$_2$–ZnO photocatalysts.

The Fe/TiO$_2$, Fe/ZnO, and Fe/TiO$_2$–ZnO catalysts were prepared applying the impregnation method to the systems containing TiO$_2$ (by Aldrich > 99.0% purity), ZnO (by Nuclear > 99.0% purity), and ethanol solutions of the metal precursor (Fe prevenient from FeCl$_3$, by Synth P.A). Finally, the catalysts were obtained after a 5 h (10℃/min) calcination process at 300–500℃, under static air atmosphere.

Table 1
Structure and characteristics of maxilon blue 5G [13]
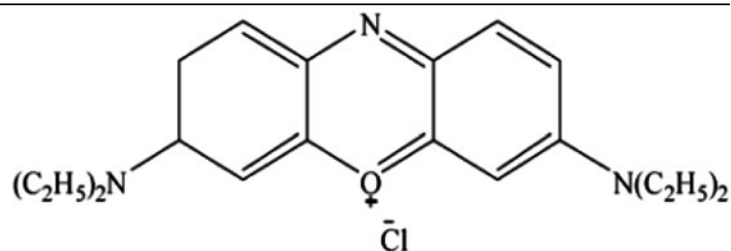
| Structure | |
| --- | --- |
|  | |
| $\lambda_{max}$ (nm) | 654 |
| $M_w$ (g mol$^{-1}$) | 266 |
| Water solubility (g L$^{-1}$) (20℃) | 40 |

## 2.2. Characterization of photocatalyst

Our study applied specific surface area, X-ray diffraction, and photoacoustic spectroscopy in the UV–vis range to characterize the developed catalysts.

### 2.2.1. Pore properties (BET Method)

Porous properties such as specific surface area, mean pore diameter, and pore volume were measured using a QUANTACHROME Analyzer—Model Nova-1200 with $N_2$ adsorption at 77 K. Both calcined and noncalcined samples were submitted to these analyses. All samples were previously submitted to a thermal treatment at 300℃ for 2 h, under vacuum, to eliminate any existing water within the pores of the solids.

### 2.2.2. X-ray diffraction

The samples were measured through a Rigaku–Denki diffractometer with Cu-Kα radiation ($\lambda$ = 1.5406 Å) at voltage of 140 V and with 40 mA current. The obtained patterns were compared against the diffraction data-set cards from the Joint Committee of Powders Diffraction Standards [18].

### 2.2.3. Thermogravimetric analyzer

Catalysts samples were analyzed using a SHIMADZU-Thermogravimetric Analyzer (TGA)—Model TGA-50; approximately 10 mg of calcined and noncalcined samples were submitted to heating at 10℃/min ramp from room temperature to 1,000℃, with nitrogen (inert gas) flowing through at 20 mL/min.

### 2.2.4. Photoacoustic spectroscopy

The photoacoustic spectroscopy measurements in the UV–vis spectral regions were performed using a state-of-the-art experimental setup. In this system, monochromatic light is provided by a 1,000-Watt xenon arc lamp (Oriel Corporation 68820) and a monochromator model 77250, also by Oriel Instruments. The light beam was modulated using a mechanical chopper—Stanford Research Systems SR540.

A lab-made photoacoustic cell was designed to have a minimal volume .The cell made of aluminum blocks and machined to hold samples with dimensions up to 5-mm diameter and 1-mm thickness, which allows light to pass through a high transparent quartz window of 6-mm diameter and 2-mm thickness.

The distance of the microphone chamber was 15 mm; it was connected to the sample holder room through a 1-mm diameter duct. A 12-mm diameter Bruel & Kjaer (model 2639) was capacitive microphone, which presents a gain of 50 mV/Pa, and flat frequency response between 1 Hz and 10 kHz. A lock-in amplifier by EG & G Instruments (model 5110) was also used. All of the photoacoustic spectra were obtained at a 20-Hz modulation frequency and recorded between 220 and 720 nm. Data were acquired using a personal computer, and the PAS spectra were normalized with respect to the carbon black signal.

The band gap energies were calculated through Eq. (6) is given as follows:

$$\lambda = \frac{hc}{E_{\text{gap}}} = \frac{1,240}{E_{\text{gap}}} \tag{6}$$

where $E_{\text{gap}}$ is the band gap energy in eV units. The direct method was applied (i.e. $m$ = 2).

## 2.3. Photocatalytic experiments

### 2.3.1. Photocatalytic reaction

The reaction mixture was transferred to a reactor consisted of a cylindrical Pyrex cell ($5.0 \times 10^{-4}$ m³) surrounded by a water jacket and a magnetic stirrer, which were used to ensure constant temperature (25℃) and solution homogeneity throughout the experiment. The tests were performed and opened to the air for 3,600 s. Oxygen was pumped at $8.3 \times 10^{-9}$ m³ s⁻¹ into the solution containing 70 ppm of reactive blue 5G dye and 1 g of the photocatalyst (2 kg m⁻³). UV light was irradiated using125-W medium pressure mercury lamp surrounded by a quartz thimble. At regular intervals of time, an aliquot of the suspension was withdrawn and filtered using a 0.45-μm Millipore filter. The discoloration of the solutions as a function of time was quantified using a spectrophotometer Shimadzu UV-1203 UV/vis.

### 2.3.2. Adsorption behavior of dyes

The adsorption tests were performed applying the same procedure, but without presence of light. Experiments in absence of photocatalysts were also conducted (i.e. photolysis only) [19].

## 2.4. ANN model development

Our study used the multilayer perceptron neural network (MLP), especially because its architecture is clear and it carries a simple mathematical formulation,

making it an easy tool for modeling and optimization. The following discussion presents the major elements of the ANN—the model structure (architecture) and the ANN training.

### 2.4.1. ANN structure selection

The origin of the ANN is the artificial intelligence. It consists of massively interconnected processing elements arranged in a layered structure. The input neurons are connected to the output neurons through layers of hidden nodes. Each neuron processes information through an activation function; hidden units with nonlinear activation function result in nonlinear mapping [20].

The foundations of the neural networks are the artificial neurons or processing elements. The neurons of the first layer have only the function of distributing the input signals for the next layers. After the input layer, the signals flow through the hidden layers until they reach the output layer, according to Eqs. (7) and (8).

If we consider a neuron "i" of layer "k", the previous layer provides this neuron with information pondered by the weight of the connections. The neuron generates a summation of these pondered inputs and the resulting value is added to an internal activation limit or bias, $w_{i,0}^{(k)}$. The resulting signal of the neuron "i" produces a response $X_i^{(k)}$ according to the activation function or transfer function $f(\bullet)$. Mathematically, this is expressed as:

$$S_i^{(k)} = w_{i,0}^{(k)} + \sum_{j=1}^{(n_{k-1})} w_{i,j}^{(k)} X_j^{(k-1)} \tag{7}$$

$$X_i^{(k)} = f\left(S_i^{(k)}\right) \tag{8}$$

A MLP with a single layer of sigmoidal hidden neurons and with a layer of linear output neurons was employed. This structure is widely applied [21] for having nonlinear processing capabilities and a universal approximation property [22].

Small random values are used in the initialization of weights and biases. Subsequently, the standard backpropagation learning algorithm [23], based on a gradient descendent method implemented in FORTRAN is employed to calibrate the ANN.

An ANN model was developed for each different catalyst applied to the discoloration of the 5G blue dye, was developed, considering 70% for training data-set and another 30% for validation data-set. Fig. 1 illustrates the considered parameters for input and output layers: time, calcination temperature, and metallic charge for input layer, and discoloration for output layer.

To build the neural networks model, we have different numbers of hidden neurons trained with the training data-set; their performances were assessed regarding the ability to make correct predictions of the validation data-set in terms of mean square error.
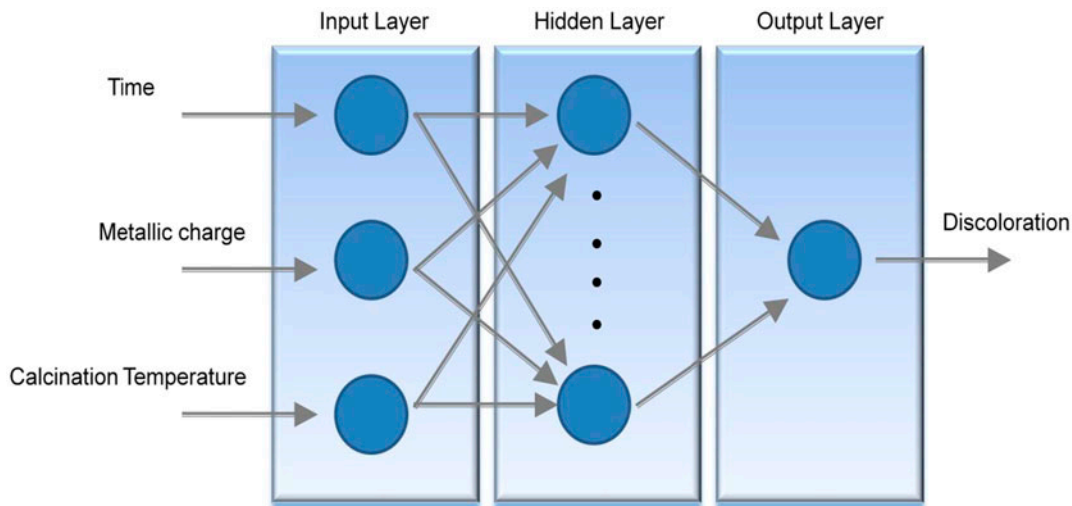


Fig 1. Artificial neural network structure.

## 3. Experimental results

Table 2 presents the results of specific surface area ($S_o$), mean pore volume ($V_p$), and average pore diameter ($d_p$) of the synthesized catalysts—calcined and noncalcined samples. Fig. 2 illustrates the alteration in the profiles of TGA and DTGA of the samples. Fig. 3 presents the catalysts diffractograms. Table 3 presents the UV–vis data. Figs. 4 and 5 show the results of the photocatalytic discoloration of the synthetic effluent. Fig. 6 provides the validation data results and ANN models developments. Tables 4, 5, and 6 present the adjustable parameters of model.

## 4. Discussion

### 4.1. Characterization

#### 4.1.1. Specific surface area, mean pore diameter, and pore volume

It was observed (Table 2) that the samples containing 1.5 and 2.5% Fe/TiO$_2$, 1.5 and 2.5% Fe/ZnO and 1.5% Fe/TiO$_2$–ZnO presented a decrease in the surface area due to particle agglomeration, heating, and pore blockage using metal [24] when increasing the calcination temperature (300–500°C). The samples with 1.5% Fe/TiO$_2$ and 2.5% Fe/ZnO calcined at 300°C presented the increased specific surface area when

compared to the area of noncalcined catalysts due to residue elimination from the pores of the material.

Regarding the metallic charge, negligible influence on the surface area of Fe–TiO$_2$ samples calcined at 300°C was observed when increasing the metal content. In contrast, when the calcination occurred at 500°C, the samples with higher Fe content presented smallest surface area. For the Fe–ZnO calcined samples, the increase in Fe content resulted in larger surface areas; for the Fe–TiO$_2$–ZnO samples calcined at 300°C, a decrease in surface area was observed when increasing the Fe content; finally, for the same samples calcined at 500°C, higher Fe content yielded larger surface areas.

### 4.2. Thermogravimetric analysis

Fig. 2 shows the TGA and DTGA data for the calcined samples (300 and 500°C) prepared with 1.5 and 2.5% Fe–TiO$_2$ (Fig. 2(A1) and (A2)); 1.5 and 2.5% Fe–ZnO (Fig. 2(B1) and (B2)); and 1.5 and 2.5% Fe–TiO$_2$–ZnO (Fig. 2(C1) and (C2)).

The 1.5% Fe/TiO$_2$ sample (Fig. 2(A1)) presented mass loss at the low temperature zone ($T_{room} \sim 150$°C) due to the elimination of adsorbed water [17]. Similar behavior was observed on the 2.5% Fe/TiO$_2$ samples (Fig. 2(A2)).

In contrast, the 1.5 and 2.5% Fe/ZnO sample (Fig. 2(A2)) revealed a significant decrease in mass

Table 2
$S_o$, $V_p$, and $d_p$ values of the synthesized catalysts

| Catalysts | % (wt) | Thermal treatment (°C) | Specific surface area, $S_o$ (m$^2$/g) | Pore volume (cm$^3$/g) | Average pore diameter (Å) |
|---|---|---|---|---|---|
| Fe/TiO$_2$ | 1.5 | Non-calcined | 0.899 | $1.342 \times 10^{-3}$ | 59.74 |
| | | 300°C | 3. 039 | $1.339 \times 10^{-3}$ | 17.62 |
| | | 500°C | * | * | * |
| | 2.5 | Non-calcined | 3.300 | $4.657 \times 10^{-3}$ | 56.45 |
| | | 300°C | 3.004 | $4.513 \times 10^{-3}$ | 61.09 |
| | | 500°C | 2.655 | $3.939 \times 10^{-3}$ | 59.36 |
| Fe/ZnO | 1.5 | Non-calcined | 9.781 | $9.707 \times 10^{-3}$ | 39.70 |
| | | 300°C | 8.162 | $1.130 \times 10^{-2}$ | 55.38 |
| | | 500°C | 2.041 | $2.818 \times 10^{-3}$ | 55.22 |
| | 2,5 | Non-calcined | 6.421 | $5.552 \times 10^{-3}$ | 34.59 |
| | | 300°C | 13.35 | $1716 \times 10^{-2}$ | 51.41 |
| | | 500°C | 5.715 | $8.440 \times 10^{-3}$ | 59.09 |
| Fe/TiO$_2$–ZnO | 1.5 | Non-calcined | 5.374 | $2.841 \times 10^{-3}$ | 21.21 |
| | | 300°C | 6.229 | $1.025 \times 10^{-2}$ | 65.81 |
| | | 500°C | 0.7622 | $8.067 \times 10^{-4}$ | 42.34 |
| | 2.5 | Non-calcined | 11.31 | $1.113 \times 10^{-2}$ | 39.37 |
| | | 300°C | * | * | * |
| | | 500°C | 4.964 | $6.548 \times 10^{-3}$ | 52.77 |

*Not possible to detect the results with the equipment used.
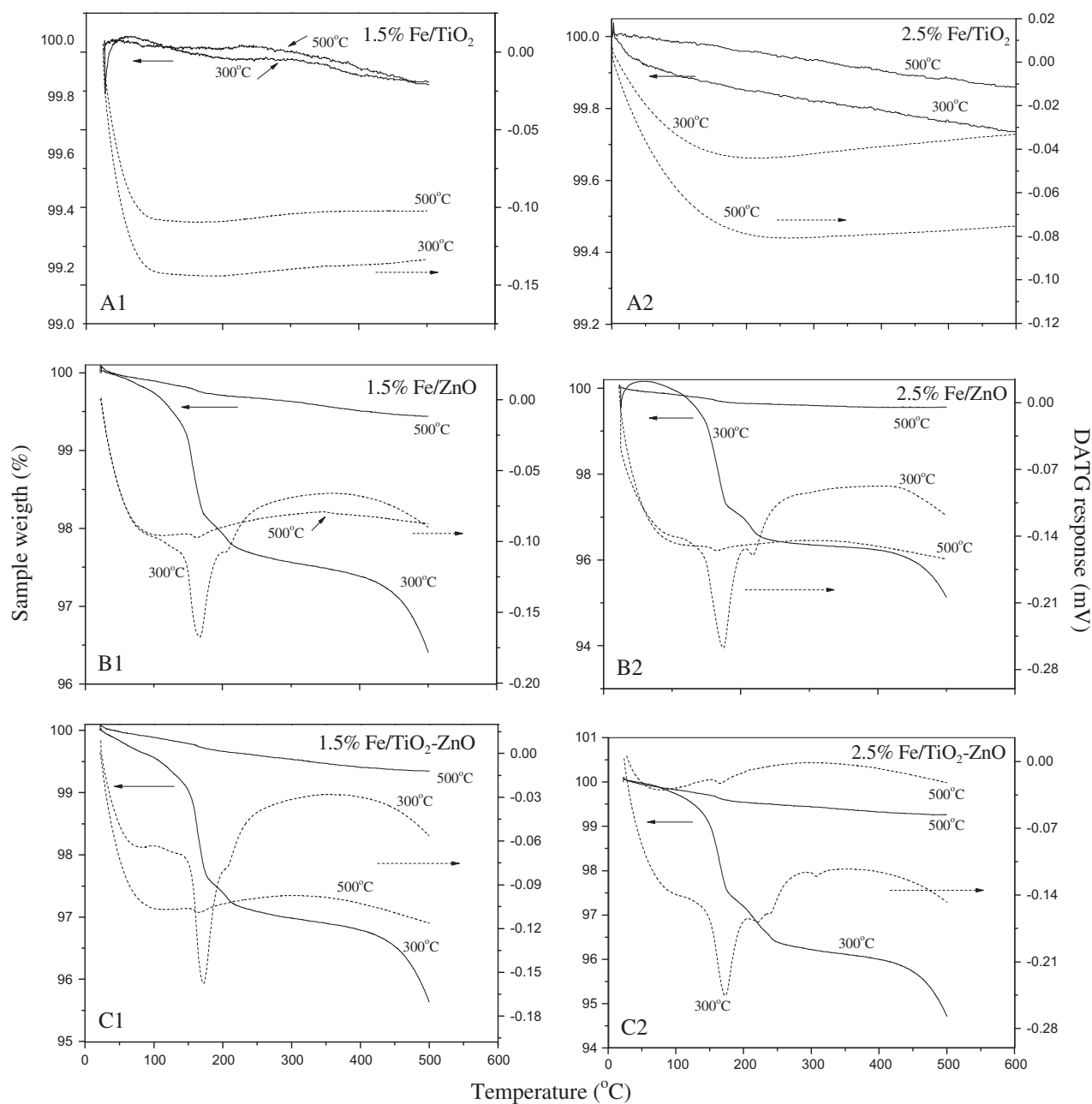
Fig. 2. TGA/DTGA data for: (A1) 1.5% Fe–TiO$_2$, (A2) 2.5% Fe–TiO$_2$, (B1) 1.5% Fe–ZnO, 2.5% Fe–ZnO, (C1) 1.5% Fe–TiO$_2$–ZnO and (C2) 2.5% Fe–TiO$_2$–ZnO calcined samples.

which was even larger for samples calcined at 300°C. The 1.5% Fe/ZnO sample calcined at 300°C (Fig. 2(B1)) presented peak with maximum value at 165°C corresponding to the total mass loss of 4%. Similarly, with the increased metallic charge sample—2.5% Fe/ZnO (Fig. 2(B2))—a maximum was observed at, with the total mass loss of 4.5%. The 1.5 and 2.5% samples calcined at 500°C suffered

a total mass loss of 0.6 and 0.5%, respectively, proving the efficiency of the thermal treatment (calcination).

As expected, the Fe/TiO$_2$–ZnO samples (Fig. 2(C1) and (C2)) presented higher mass loss when calcined at 300°C. The total mass loss was 4.5 and 6.5% for the 1.5 and 2.5% samples, respectively. For these samples, the highest mass loss occurred in the low temperature
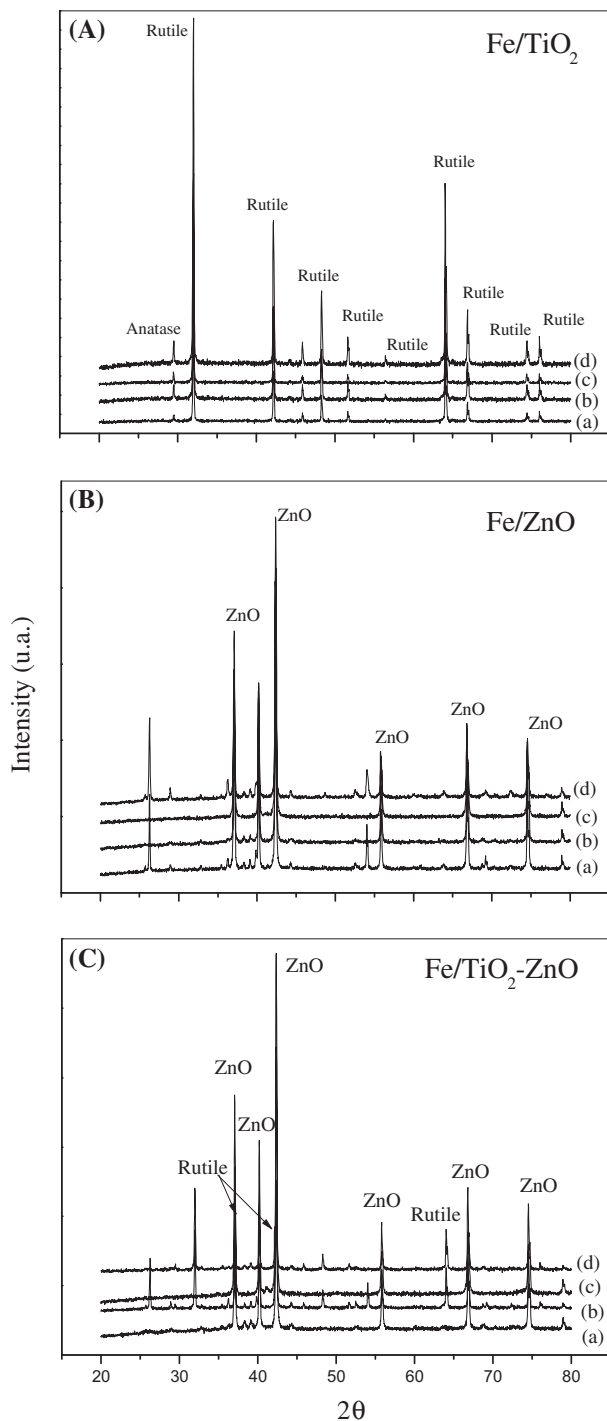
Fig. 3. XRD pattern of the samples (A) Fe–TiO₂ [(a) 1.5% Fe/ TiO₂ (300°C), (b) 1.5% Fe/TiO₂ (500°C), (c) 2.5% Fe/ TiO₂ (300°C), and (d) 2.5% Fe/TiO₂ (500°C)]; (B) Fe–ZnO [(a) 1.5% Fe/ZnO (300°C), (b) 1.5% Fe/ZnO (500°C), (c) 2.5% Fe/ZnO (300°C), and (d) 2.5% Fe/ZnO (500°C)]; and (C) Fe/ZnO–TiO₂ [(a) 1.5% Fe/ZnO–TiO₂ (300°C), (b) 1.5% Fe/ Fe/ZnO–TiO₂ (500°C), (c) 2.5% Fe/ Fe/ZnO–TiO₂ (300°C), and (d) 2.5% Fe/ Fe/ZnO–TiO₂ (500°C)].

zone ($T_{room} \sim 200$°C). In addition, the samples calcined at 500°C presented similar behavior of the Fe/ZnO catalyst (at the same conditions), with approximate mass loss of 0.7% (1.5% Fe/TiO₂–ZnO) and 0.6% (2.5% Fe/TiO₂–ZnO).

## 4.3. X-ray diffraction

Fig. 3 illustrates the diffractograms of the 1.5% Fe/TiO₂ calcined catalysts (300 and 500°C—Fig. 3((A), (a) and (b), respectively). Crystalline structures and increased peaks intensity at high temperatures was observed.

In contrast, no significant variation was detected when increasing the metallic charge (1.5–2.5% (Fig. 3(A), (c) and (d), respectively). Anatase and rutile species were intensified; some authors claim that the anatase phase is ideal for photocatalysis [25–27]; however, recent studies have revealed that both the rutile and the anatase phase present high photocatalytic activity [28].

Differences in lattice structures of anatase and rutile TiO₂ yield varied densities and electronic band structures, which lead to different band gaps (for bulk materials: anatase 3.20 eV and rutile 3.02 eV) [29,30]. Therefore, the absorption thresholds correspond to 384 and 410-nm wavelengths for both titania forms, respectively. We also observed that the addition of metal resulted in absorption thresholds displacements for all studied samples (Table 3). The X-ray diffraction of material 1.5 and 2.5% Fe/ZnO (Fig. 3(B)) revealed that only species of ZnO were found. The sample 2.5% Fe/ZnO presents the same behavior. Fig. 3(C) illustrates the diffractograms for samples 1.5 and 2.5% Fe/TiO₂–ZnO; ZnO, TiO₂ presented rutile form. For all samples, iron presented no corresponding crystalline phases for being highly dispersed.

## 4.4. Photoacoustic spectroscopy

Data collected from UV–vis revealed different values of energy gap in the photocatalyst, depending on the calcination temperature and doped system (Table 3). By comparing the band gap value of commercial TiO₂ (3.12, calcined at 500°C, and 3.13, calcined at 350°C) [31] against TiO₂ doped with Fe, the later presented the lowest value. Band gap from alterations in the semiconductor such as the dopant may result in crystal imperfection [32]. Except for Fe/TiO₂, the increase in metallic charge implied an increase in band gap for both the calcination temperature cases. Also, significant influence of calcination temperature

Table 3
Photoacoustic spectroscopy

| Catalyst | % (wt) | Calcination temperature | | | |
| | | 300(℃) | | 500(℃) | |
| | | Band gap (eV) | Absorption threshold (nm) | Band gap (eV) | Absorption threshold (nm) |
|---|---|---|---|---|---|
| Fe/TiO$_2$ | 1.5 | 2.60 | 476 | 2.79 | 444 |
| | 2.5 | 2.57 | 482 | 2.41 | 514 |
| Fe/ZnO | 1.5 | 2.51 | 494 | 2.55 | 486 |
| | 2.5 | 2.78 | 446 | 2.92 | 421 |
| Fe/TiO$_2$–ZnO | 1.5 | 2.59 | 478 | 2.59 | 478 |
| | 2.5 | 2.75 | 451 | 2.83 | 438 |

Table 4
Adjust parameter for Fe/TiO$_2$ using ANN model

| | $W_{0j}^{k}$ | $W_{0j}^{k+1}$ | $W_{1j}^{k}$ | $W_{2j}^{k}$ | $W_{3j}^{k}$ | $W_{1j}^{k+1}$ |
|---|---|---|---|---|---|---|
| $j = 1$ | −6.786 | 1.730 | 2.096 | −6.513 | −0.186 | −26.071 |
| $j = 2$ | 86.854 | * | 8.501 | −3.936 | 0.483 | −2.559 |
| $j = 3$ | 0.038 | * | −0.505 | 20.071 | 27.844 | −1.476 |

*There is no associated value.

Table 5
Adjust parameter for Fe/ZnO using ANN model

| | $W_{0j}^{k}$ | $W_{0j}^{k+1}$ | $W_{1j}^{k}$ | $W_{2j}^{k}$ | $W_{3j}^{k}$ | $W_{1j}^{k+1}$ |
|---|---|---|---|---|---|---|
| $j = 1$ | −9 | 7 | 18 | −12 | 0.478 | −16 |
| $j = 2$ | 55 | * | −0.086 | −6 | 4 | −2 |
| $j = 3$ | 5 | * | −0.505 | 16 | 19 | −3 |

*There is no associated value.

Table 6
Adjust parameter for Fe/TiO$_2$–ZnO using ANN model

| | $W_{0j}^{k}$ | $W_{0j}^{k+1}$ | $W_{1j}^{k}$ | $W_{2j}^{k}$ | $W_{3j}^{k}$ | $W_{1j}^{k+1}$ |
|---|---|---|---|---|---|---|
| $j = 1$ | −9 | 9 | −0.081 | −7 | 0.053 | −18 |
| $j = 2$ | 67 | * | 18 | −6 | 5 | −2 |
| $j = 3$ | 5 | * | −0.080 | 18 | 21 | −2 |

*There is no associated value.

on the 2.5% Fe/ZnO photocatalyst was observed, (from 2.78 to 2.92 eV).

### 4.5. Photocatalytic behavior

Figs. 4 and 5 illustrate the photocatalytic discoloration and adsorption results of synthetic effluent containing reactive blue dye 5G for Fe/TiO$_2$, Fe/ZnO, and Fe/TiO$_2$–ZnO catalysts regarding different metallic charges and calcination temperatures. . The values revealed that, in this case, the photocatalytic discoloration in an aqueous solution can be described through a first-order-kinetic model, $\ln(C_0/C) = kt$, where $C_0$ is initial concentration and $C$ is concentration at any time $t$.

All catalysts provided full discoloration of the reaction system. Greater efficiency time for catalysts calcined at 300℃ was observed.

Fe–TiO$_2$ and Fe–ZnO (~40 min) catalysts required shorter time for total discoloration (100%) as well as Fe–TiO$_2$–ZnO (~50 min) catalysts calcined 300℃ for 1.5 and 2.5% Fe. The Fe–ZnO catalyst presented the largest surface area (8.162 m$^2$/g), and the smallest band gap (2.51 eV), justifying the behavior. Nonetheless, the Fe–TiO$_2$ catalyst obtained the smallest surface area and the largest band gap (2.60 eV). In addition, Fe–TiO$_2$ catalysts presented structure containing rutile and similar behavior under such conditions.

In contrast, a different behavior with the increase in calcination temperature was observed (Fig. 4(B)). The Fe–ZnO catalyst presented the shortest time required for the total discoloration (40 min); its band gap was smaller (2.55 eV) than the Fe–TiO$_2$ (2.79 eV— total discoloration time ~80 min) and the Fe–TiO$_2$– ZnO (2.59 eV—total discoloration time ~ 80 min) catalysts.

Fig. 5(A) (calcined at 300℃) and (B) (calcined at 500℃) illustrate the behavior of catalysts with nominal charge of 2.5% wt. We observed the significant difference between Fe/ZnO calcined at 300℃, with the most satisfactory discoloration time (~30 min.), and the same sample calcined at 500℃ (~50 min.), which presented the highest discoloration time. This fact indicates the occurrence of nonfavorable structural alteration to photocatalysis when the catalyst was calcined at 500℃.

This catalyst also presented an increase in band gap upon calcination at higher temperatures, going from 2.78 eV (calcined at 300℃) to 2.92 eV (calcined at 500℃). Comparing Fig. 5(A) and (B), a greater time
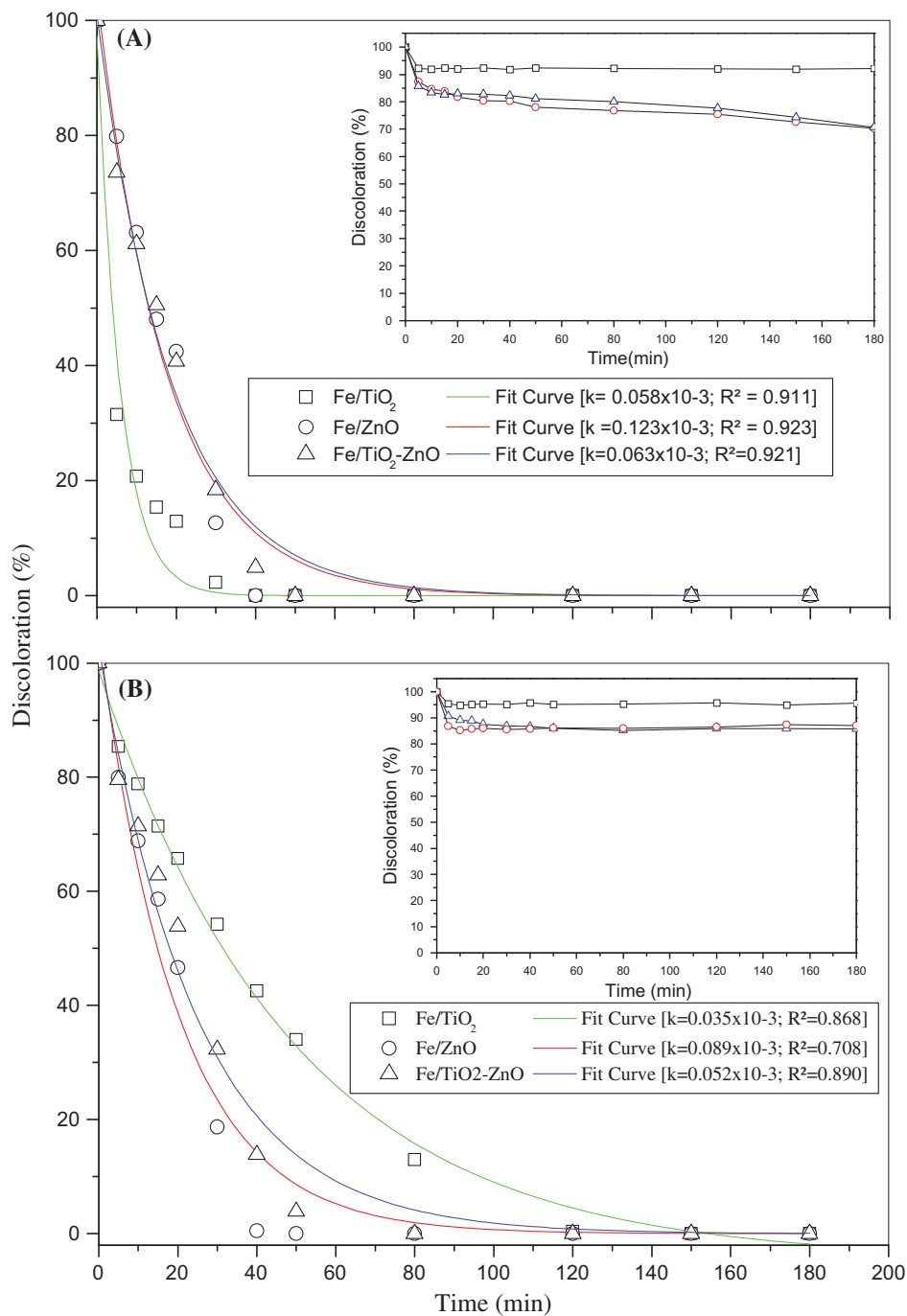
Fig. 4. Photocatalytic discoloration of blue 5G dye content 1.5% wt. Fe for Fe–TiO$_2$, Fe–TiO$_2$–ZnO, and Fe–ZnO photocatalysts calcined at (A) 300°C and (B) 500°C. (in detail adsorption test).

required for complete discoloration can be noticed when the catalyst was calcined at 500°C.

The adsorption on the catalysts surface was, in general, favorable for catalysts with higher Fe content (Fig. 5), which probably occurred due to their increased surface areas.

### 4.6. Artificial neural network model

Fig. 6 illustrates the results for the photocatalytic discoloration ANN Models of synthetic effluent containing reactive blue dye 5G and Fe/TiO$_2$, Fe/ZnO or Fe/TiO$_2$–ZnO catalysts with various metallic
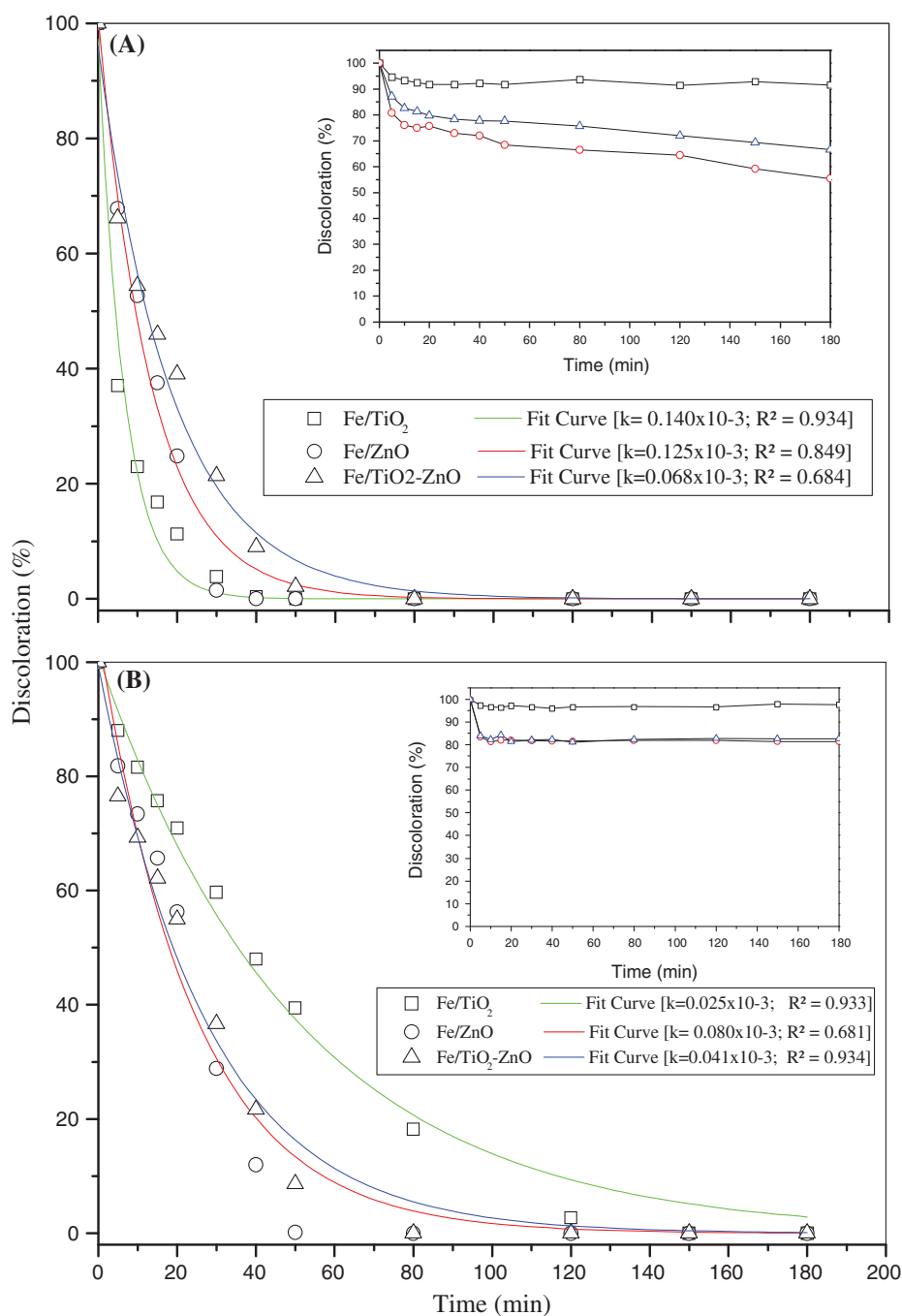
Fig. 5. Photocatalytic discoloration of blue 5G dye content 2.5% wt. Fe for Fe–TiO$_2$, Fe–TiO$_2$–ZnO, and Fe–ZnO photocatalysts calcined at (A) 300℃ and (B) 500℃ (in detail adsorption test).

charges and calcination temperatures. It also illustrates the comparison between the experimental adsorption and the ANN Model results. The input values for the ANN model were the time discoloration, the calcination temperature, and the metallic charge; the output value was the discoloration magnitude.

For the evaluated ANN models with different numbers of hidden neurons, better results were observed with three hidden neurons. A larger number of neurons only increase the time computational.

Tables 4–6 present the ANN models for catalyst Fe/TiO$_2$, Fe/ZnO, and Fe/TiO$_2$–ZnO. All of the models developed with three neurons hidden layer used
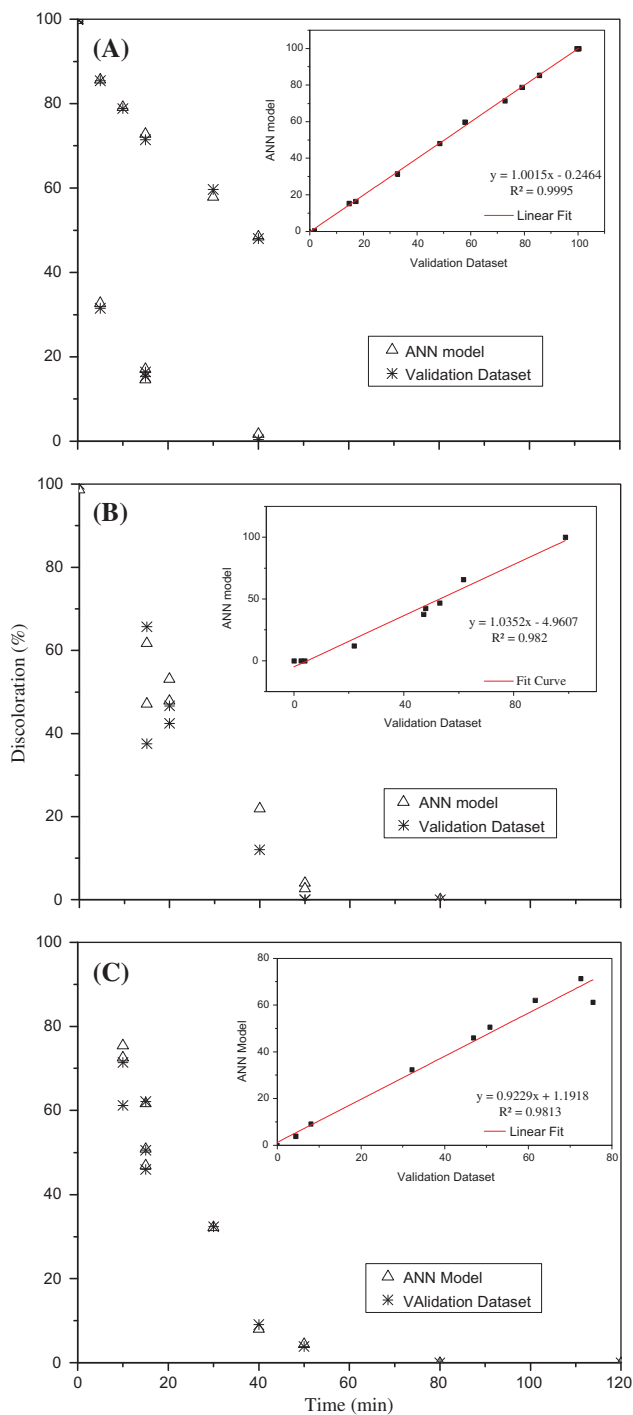
Fig. 6. ANN model discoloration for catalysts (A) Fe/TiO$_2$, (B) Fe/ZnO, and (C) Fe/TiO$_2$–ZnO (in detail: correlation coefficient for ANN model).

four bias—three for the intermediate layer ($W_{0j}^{k}$), one for the output layer ($W_{0j}^{k+1}$). In addition, this layer had twelve weights adjusted—nine are connection parameters with the input layer ($k-1$) and the neurons of the

intermediate layer ($k$); the remaining three were parameters connecting the intermediate layer with the output layer ($k + 1$).

Fig. 6(A) illustrates the results of the discoloration of catalysts Fe/TiO$_2$; the ANN model and validation data. The model presented an excellent result representing very accurate data.

Fig. 6(B) brings the results for the discoloration using catalyst Fe/ZnO; the values were satisfactory but did not present the same performance of the neural model for the discoloration with catalyst Fe/TiO$_2$. It happened because the number of experimental data with values differs from zero—catalyst Fe/TiO$_2$—the discoloration occurs more slowly and generates more experimental data to train and validate the networks.

Fig. 6(C) presents the results for catalysts Fe/TiO$_2$–ZnO; they presented intermediate discoloration, that is, it was not as slow as the discoloration obtained for catalyst Fe/TiO$_2$, and not as fast as the discoloration obtained for Fe–ZnO. Therefore, the generated model presented good representativity for the validation data.

An alternative to validate the generated neural models is to relate the generated data through the neural and validation models to a line of tendency and establishment of the correlation coefficient ($R^2$). In that case, the obtained correlation coefficients were $R^2$: 0.99947, 0.98202, and 0.98126 for neural models Fe/TiO$_2$, Fe/ZnO, and Fe/TiO$_2$–ZnO, respectively. The details in the Fig. 6 present the results for the neural model with the lowest correlation coefficient.

## 5. Conclusions

The results obtained from photocatalytic tests revealed that, under the tests conditions, nominal metallic charge, calcination temperature, and the type of oxide influenced the photocatalytic discoloration of the synthetic effluent containing reactive blue dye 5G. All catalysts provided the total discoloration of the reaction medium. When calcined at 300°C, Fe–TiO$_2$–ZnO presented better discoloration efficiency than Fe–TiO$_2$ and Fe–ZnO. However, when calcined at 500°C the following ranking, based on the amount of time required for complete discoloration, was obtained: Fe–ZnO < Fe–TiO$_2$–ZnO < Fe–TiO$_2$. In addition, it was observed that, with the increase in metallic charge from 1.5 to 2.5% wt. Fe, both Fe–TiO$_2$ and Fe–ZnO catalysts (calcined at 300°C) maintained the same discoloration time (40 min); however, the catalyst containing mixed oxides (TiO$_2$–ZnO) required the highest amount of time to reach total discoloration of the medium 80 min. Moreover, the increase in calcination temperature (500°C) resulted in the increase in

total discoloration time. We emphasize that the 30 min increase in discoloration time for the Fe–TiO$_2$ catalyst only with the increase in metallic charge as the most significant difference under the same conditions.

Finally, the most satisfactory structure to build the neural models was composed of three neurons of the intermediate layer. The ANNs can be successfully employed to build discoloration models for the studied catalysts ($R^2$ ranging 0.99947–0.98202). Even when a reduced number of experimental data is available for training and testing the networks, the model still maintains the good performance.

## References

[1] L.M.S. Colpini, H.J. Alves, O.A.A. Santos, C.M.M. Costa, Discoloration and degradation of textile dye aqueous solutions with titanium oxide catalysts obtained by the sol-gel method, Dyes Pigments 76 (2008) 525–529.

[2] C.C.I. Guaratini, M.V.B. Zanoni, Corantes têxteis (Textiles Dyes), Química Nova 23 (2000) 71–78.

[3] Y. Sürme, R.F. Yılmaz, K. Kayakırılmaz, Removal of textile dye Lanaset Red G from waters by electrochemical degradation and spectrophotometric determination, Desalin. Water Treat. 53 (2015) 524–529.

[4] A. Mills, S. Le Hunte, An overview of semiconductor photocatalysis, J. Photochem. Photobiol. A 108 (1997) 1–35.

[5] A. Vidal, Z. Dinya, F. Mogyorodi Jr., Photocatalytic degradation of thiocarbamate herbicide active ingredients in water, Appl. Catal., B. 21 (1999) 259–267.

[6] A.A. Khodja, T. Sehili, J.F. Pilichowski, P. Boule, Photocatalytic degradation of 2-phenylphenol on TiO$_2$ and ZnO in aqueous suspensions, J. Photochem. Photobiol., A. 141 (2001) 231–239.

[7] E. Kusvuran, A. Samil, O.M. Atanur, O. Erbatur, Photocatalytic degradation kinetics of di- and tri-substituted phenolic compounds in aqueous solution by TiO$_2$/UV, Appl. Catal., B. 58 (2005) 211–216.

[8] N. Daneshvar, S. Aber, M.S. Seyeddorraji, A.R. Khataee, M.H. Rasoulifard, Photocatalytic degradation of the insecticide diazinon in the presence of prepared nanocrystalline ZnO powders under irradiation of UV-C light, Sep. Purif. Technol., 58 (2007) 91-98.

[9] M.R. Hoffmann, S.T. Martin, W.Y. Choi, D.W. Bahnemann, Environmental applications of semiconductor photocatalysis, Chem. Rev. 95 (1995) 69–96.

[10] Y.L. Dong, J.L. Won, S. Jae Sung, H.K. Jung, S.K. Yang, Electronic surface state of TiO$_2$ electrode doped with transition metals, studied with cluster model and DV-Xα method, Comput. Mater. Sci. 30 (2004) 383–388.

[11] D. Dvoranová, V. Brezová, M. Mazúr, M.A. Malati, Investigations of metal-doped titanium dioxide photocatalysts, Appl. Catal., B. 37 (2002) 91–105.

[12] S. S.Haykin, Redes Neurais Princípios e Prática (Neural Networks: A Comprehensive Foundation), second ed., Bookman, Porto Alegre, 2001.

[13] C.A. Nunes, C.F. Lima, L.C.A. Barbosa, J.L. Colodette, P.H. Fidêncio, Determinação de constituintes químicos em madeira de eucalipto por Pi-CG/EM e calibração multivariada: comparação entre redes neurais artificiais e máquinas de vetor suporte (Determination of chemical constituents in eucalyptus wood by Py-GC/MS and multivariate calibration: Comparison between artificial neural network and support vector machines), Quím. Nova. 34 (2011) 279–283.

[14] A.R. Khataee, M. Zarei, Photocatalysis of a dye solution using immobilized ZnO nanoparticles combined with photoelectrochemical process, Desalination 273 (2011) 453–460.

[15] A.R. Khataee, M. Fathinia, M. Zarei, B. Izadkhah, S.W. Joo, Modeling and optimization of photocatalytic/photoassisted-electro fenton like degradation of phenol using a neural network coupled with genetic algorithm, J. Ind. Eng. Chem. 20 (2014) 1852–1860.

[16] S. Dutta, S.A. Parsons, C. Bhattacharjee, S.S.D. Bandhyopadhyay, Development of an artificial neural network model for adsorption and photocatalysis of reactive dye on TiO$_2$ surface, Expert Syst. Appl. 37 (2010) 8634–8638.

[17] M. Alkan, M. Doğan, Y. Turhan, Ö. Demirbaş, P. Turan, Adsorption kinetics and mechanism of maxilon blue 5G dye on sepiolite from aqueous solutions, Chem. Eng. J. 139 (2008) 213–223.

[18] JCPDS International Centre for Diffraction Data, Powder Diffration File, JCPDS-ICDD, Newtown Sq, PA, 2003.

[19] A. Rezaee, M.T. Ghaneian, S.J. Hashemian, G. Moussavi, A. Khavanin, G. Ghanizadeh, Decolorization of reactive blue 19 dye from textile wastewater by the UV/H$_2$O$_2$ process, J. Appl. Sci. 8 (2008) 1108–1112.

[20] D.C. Psichogios, L.H. Ungar, Direct and indirect model based control using artificial neural networks, Ind. Eng. Chem. Res. 30 (1991) 2564–2573.

[21] B. Dębska, B. Guzowska-Świder, Application of artificial neural network in food classification, Anal. Chim. Acta. 705 (2011) 283–291.

[22] G. Cybenko, Approximation by superpositions of a sigmoidal function, Math. Control Systems Signals. 2 (4) (1989) 303–314.

[23] C.M. Bishop, Neural networks for pattern recognition, Oxford University Press, Oxford, 1995.

[24] G.G. Lenzi, M.K. Lenzi, M.L. Baesso, A.C. Bento, L.M.M. Jorge, O.A.A. Santos, Cobalt, nickel and ruthenium-silica based materials synthesized by the sol-gel method, J. Non-Cryst. Solids. 354 (2008) 4811–4815.

[25] R.T. Tayade, P.K. Surolia, R.G. Kulkarni, R.V. Jasra, Photocatalytic degradation of dyes and organic contaminants in water using nanocrystalline anatase and rutile TiO$_2$, Sci. Technol. Adv. Mater. 8 (2007) 455–462.

[26] S. Bakardjieva, J. Šubrt, V. Štengl, M.J. Dianez, M.J. Sayagues, Photoactivity of anatase-rutile TiO$_2$ nanocrystalline mixtures obtained by heat treatment of homogeneously precipitated anatase, Appl. Catal., B. 58 (2005) 193–202.

[27] H.G. Roy, Comparison of photocatalytic activities of anatase and rutile titania nanostructures synthesized by microwave irradiation, Res. Appl. Mater. 6 (2013) 65–72.

[28] Q. Sun, Y. Xu, Evaluating intrinsic photocatalytic activities of anatase and rutile TiO$_2$ for organic degradation in water, J. Phys. Chem. C. 114 (2010) 18911–18918.

[29] A. Fujishima, K. Hashimoto, T. Watanabe, TiO$_2$ photo-catalysis. Fundments and applications, first ed., BKC, Tokyo, 1999.

[30] D. Mardare, G.I. Rusu, The influence of heat treatment on the optical properties of titanium oxide thin films, Mater. Lett. 56 (2002) 210–214.

[31] G.G. Lenzi, C.V.B. Fávero, L.M.S. Colpini, H. Bernabe, M.L. Baesso, S. Specchia, O.A.A. Santos, Photocatalytic reduction of Hg(II) on TiO$_2$ and Ag/TiO$_2$ prepared by the sol–gel and impregnation methods, Desalination 270 (2011) 241–247.

[32] M. Arshad, A. Azam, A.S. Ahmed, S. Mollah, A.H. Naqvi, Effect of co substitution on the structural and optical properties of ZnO nanoparticles synthesized by sol-gel route, J. Alloys Compd. 509 (2011) 8378–8381.